ACS NANO

www.acsnano.org

ARTICLE

Advancing the Boundaries of Immunotherapy in Lung Adenocarcinoma with Idiopathic Pulmonary Fibrosis by a Biomimetic Proteinoid Enabling Selective Endocytosis

Aimin Jiang, Xiaoqiang Zheng, Siqi Yan, Jin Yan,* Yu Yao,* and Wangxiao He*

Cite This: *ACS Nano* 2024, 18, 5358–5373

Read Online

ACCESS | Metrics & More | Article Recommendations | Supporting Information

ABSTRACT: The coexistence of lung adenocarcinoma (LUAD) with idiopathic pulmonary fibrosis (IPF), which has been extensively documented as a prominent risk factor for checkpoint inhibitor-related pneumonitis (CIP) in patients undergoing immunotherapy, has long been considered a restricted domain for the use of immune checkpoint inhibitors (ICIs). To overcome it, an approach was employed herein to specifically target PD-L1 within the cellular interior, surpassing the conventional focus solely on the cytomembrane, thereby facilitating the development of ICIs capable of distinguishing between LUAD cells and noncancerous cells based on their distinctive endocytic propensities. By exploiting the aurophilicity-driven self-assembly of a PD-L1 binding peptide (PDBP) and subsequently encapsulating it within erythrocyte membranes (EM), the resulting biomimetic ICIs protein EMS-PDBP exhibited extraordinary selectivity in internalizing LUAD cells, effectively targeting PD-L1 within cancer cells while hindering its membrane translocation. The EMS-PDBP treatment not only reactivated the antitumor immune response in the LUAD orthotopic allograft mouse model but also demonstrated a favorable safety profile by effectively eliminating any immune-related adverse events (irAEs). Most significantly, EMS-PDBP successfully and safely restored the antitumor immune response in a mouse model of LUAD with coexistent IPF, thus shattering the confines of ICIs immunotherapy. The reported EMS-PDBP collectively offers a potential strategy for immune reactivation to overcome the limitations of immunotherapy in LUAD coexisting with IPF.

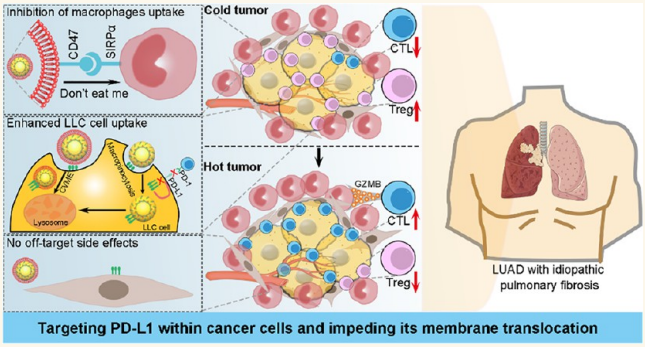

KEYWORDS: *biomimetic supramolecular, immunotherapy, lung adenocarcinoma, idiopathic pulmonary fibrosis, immune-related adverse events*

INTRODUCTION

Since the emergence of immune-oncology, the treatment trajectory and natural progression of advanced malignant tumors have undergone a significant revolution.[1] The undeniable superiority of immune checkpoint inhibitors (ICIs) over conventional chemotherapy has been unequivocally demonstrated in both the initial treatment and subsequent courses of therapy.[2−5] Particularly in the case of lung adenocarcinoma (LUAD), ICIs targeting the programmed cell death protein 1 (PD-1)/programmed death-ligand 1 (PD-L1) axis have shown tremendous promise in extending the lives of patients without driver gene mutations.[6−10] The hopes of their survival, however, are consistently thwarted by checkpoint inhibitor-related pneumonitis (CIP),[11] which afflict approximately 20% of individuals with LUAD.[11−13] The presence of preexisting interstitial lung disease (ILD), particularly idiopathic pulmonary fibrosis (IPF), has been extensively documented as a prominent risk factor for CIP in LUAD patients undergoing ICIs treatment.[8,11,12] Therefore, the coexistence of LUAD and IPF has long been regarded as a restricted domain for ICIs.

Received: October 10, 2023
Revised: January 31, 2024
Accepted: February 1, 2024
Published: February 6, 2024

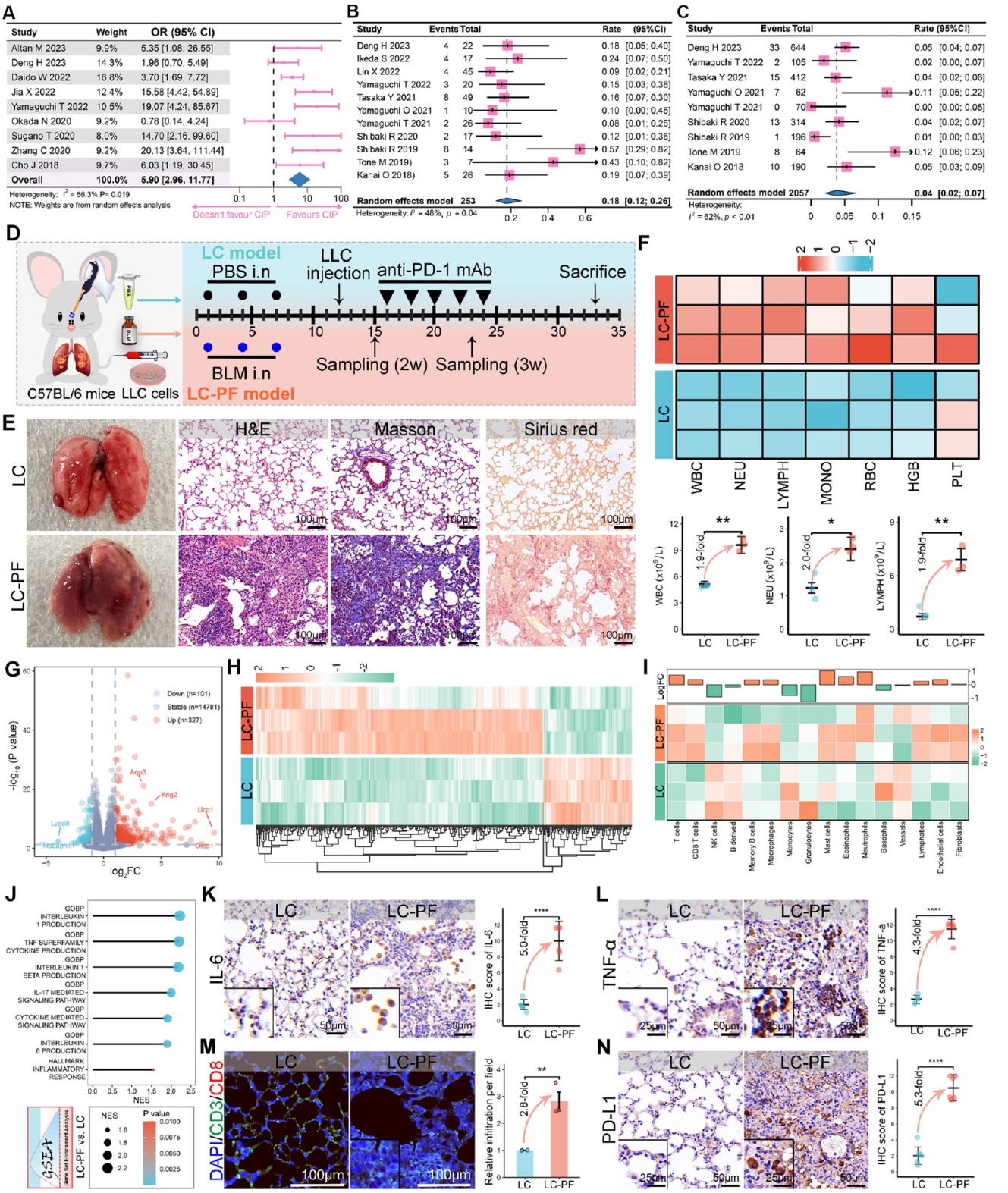

Figure 1. Anti-PD-1 mAb therapy significantly increased the inflammatory response in an orthotopic mouse model of LUAD with IPF. (A) Forest plots depicting the pooled analysis of the correlation between pre-existing interstitial lung disease (ILD) and any grade of checkpoint inhibitor-related pneumonitis (CIP) in lung cancer patients. (B,C) Pooled analysis demonstrating the occurrence of severe grade (≥grade 3) CIP in lung cancer patients with (B) and without (C) preexisting ILD. (D) Schematic illustrating the establishment and intervention of the lung adenocarcinoma (LUAD) orthotopic murine (termed the LC) model and the LUAD tumor-bearing idiopathic pulmonary fibrosis (IPF) (termed the LC-PF) model. (E) Representative photograph, H&E staining, Masson staining, and Sirius red staining of mouse lung tissue after five successive cycles of anti-PD-1 mAb treatment. (F) Blood routine test results for LC and LC-PF mice. The upper panel presents a scaled heatmap showing peripheral blood leukocytes (WBC), neutrophils (NEU), lymphocytes (LYMPH), monocytes (MONO), red blood cells (RBC), hemoglobin (HGB), and platelet (PLT) levels in the indicated groups. The lower panel provides statistical analysis of WBC, NEU, and LYMPH between different groups (n = 3, mean ± SD). (G,H) Volcano plot (G) and hierarchical clustering heatmap (H) of

https://doi.org/10.1021/acsnano.3c09852
ACS Nano 2024, 18, 5358−5373

Figure 1. continued

differentially expressed genes (DEGs) identified in the normal lung samples between the LC and LC-PF groups after anti-PD-1 mAb intervention. (I) Heatmap illustrating the infiltration levels of 16 immune and stromal cell types estimated using the mMCP-counter algorithm across different groups. The infiltration values underwent normalization. Log (fold change) of immune and stromal cells in different groups was calculated to reflect their alteration. (J) Gene set enrichment analysis (GSEA) revealed significantly altered pathways between LC and LC-PF groups, encompassing pathways related to proinflammatory cytokine production and inflammatory response. (K,L) Representative immunohistochemistry (IHC) images and corresponding statistical results for IL-6 (K) and TNF-α (L) levels in the indicated groups after anti-PD-1 mAb treatment (n = 3, mean ± SD). (M) Representative confocal images and statistical analysis of $CD3^+/CD8^+$ T cells in LC and LC-PF groups (n = 3, mean ± SD). (N) Representative IHC images and statistical analysis of PD-L1 levels in the pulmonary mesenchyme among different groups (n = 3, mean ± SD). *P < 0.05; **P < 0.01; ****P < 0.0001.

Recent research has revealed that the perplexing CIP is caused by abnormal activation of immune cells in pulmonary mesenchyme, rather than being solely attributed to lung neoplasms.[14,15] In this scenario, the stimulation of immune killer cells, particularly cytotoxic T cells, would culminate in the obliteration of noncancerous cells, leading to a severe inflammatory response in lung and subsequent compelled discontinuation of ICIs.[14,15] The aforementioned process is intricately intertwined with the widely employed anti-PD-1 therapy in clinical settings, effectively impeding the immunosuppressive interaction between T-cellular PD-1 and both cancerous PD-L1 as well as noncancerous PD-L2 (B7-DC), encompassing their presence on the surface of lung fibroblasts and macrophages.[16−19] Furthermore, therapeutic intervention of PD-1/PD-L1 by neutralizing antibodies still elicits immune inflammation within the pulmonary mesenchyme, as evidenced by the current findings in this study (Figure 1), presumably attributable to the heightened expression of PD-L1 in lung fibroblasts. Therefore, the crucial task persists in precisely targeting neoplastic PD-L1 within tumors, all the while safeguarding the intricate immune balance in areas beyond the tumor site, especially within the highly susceptible region prone to CIP—pulmonary mesenchyme.

In the pursuit of this objective, a groundbreaking approach was employed in this study to specifically target PD-L1 within the cellular interior rather than solely on the cytomembrane, thereby enabling the development of ICIs that can distinguish between LUAD cells and noncancerous cells based on their distinctive endocytic propensities. In detail, owing to the requirement for endocytogenic antigens, macrophages efficiently internalize proteins through macropinocytosis, while tumor cells rely on both macropinocytosis and caveolae-dependent cellular endocytosis for nutritional plunder.[20] Meanwhile, lung fibroblasts uptake proteins through clathrin-dependent cellular uptake, ensuring maximum selectivity of the internalized proteins.[21] Hence, it can be postulated that the development of an ICIs protein exhibiting a predilection for caveolae-mediated cellular endocytosis could potentially facilitate its selective internalization into tumor cells rather than into macrophages and lung fibroblasts. The verification was accomplished through the construction of a biomimetic ICIs protein, achieved by the exquisite aurophilicity-driven self-assembly[22−25] of PD-L1 binding peptide (PDBP) and subsequent encapsulation within erythrocyte membranes (EM). The escalating number of peptide-conjugated gold nanoparticles (AuNPs) has been developed and applied for clinical trials due to its inherent advantages, including essential inertness, minimal toxicity, and cost-effectiveness.[22,23,25,26] The encapsulation of EM has been reported to alter the internalization tendency of nanoparticles, shifting from macropinocytosis to caveolae-mediated cellular endocytosis.[27] The erythrocyte-membrane-disguised supramolecular PDBP (EMS-PDBP) exhibited good selectivity in internalizing cells, subsequently targeting PD-L1 within cancer cells and impeding its membrane translocation. As a result, the EMS-PDBP treatment not only reactivated the antitumor immune response in the LUAD orthotopic allograft mouse model established with a mouse LUAD cell line but also exhibited a favorable safety profile by effectively eliminating any immune-related adverse events (irAEs). More significantly, EMS-PDBP effectively and safely restore the antitumor immune response in a mouse model of LUAD with coexistent IPF, thereby shattering this confined realm of ICIs immunotherapy.

RESULTS AND DISCUSSION

The Blockade of the PD-1/PD-L1 Axis Significantly Augments the Inflammatory Response in an Orthotopic Mouse Model of LUAD with Idiopathic Pulmonary Fibrosis (IPF). Recently, immunotherapy represented by an immune checkpoint blockade (ICB) has profoundly altered the treatment landscape of lung cancer, delivering substantial survival advantages to patients. Nonetheless, its wide application was hindered by irAEs, such as CIP. Existing evidence indicates a notable association between preexisting ILD and an increased occurrence of CIP in patients with lung cancer.[11,28−30] Here, we first investigated the correlation between preexisting ILD and the risk of CIP in lung cancer patients undergoing ICB therapy in a Meta-analysis. A total of 28 studies with 7831 participants were included in pooled analysis after a thorough literature screening (Table S1). The pooled analysis based on a random effect model indicated that preexisting ILD is significantly correlated with the occurrence of any grade CIP in lung cancer patients (odds ratio [OR] = 5.90, 95% confidence interval [CI]: 2.96−11.77; Heterogeneity test: I^2 = 56.3%, P = 0.019, Figure 1A). Besides, it showed that both the incidence of any grade of CIP (28%: 22−35% vs 10%: 9−13%, Figure S1A,B) and severe grade of CIP (≥grade 3, 18%: 12−26% vs 4%: 2−7%, Figure 1B,C) in lung cancer patients with preexisting ILD are greater than that in them without preexisting ILD.

IPF is a prevalent subtype of ILDs. Currently, the most prevalent animal model for replicating the pathological process of human IPF involves intratracheal injection of bleomycin into C57BL/6 mice.[31] The LUAD orthotopic murine model was subsequently established in mice, with (LC-PF) or without (LC) coexistent IPF, to explore the potential mechanisms underlying CIP. First of all, 6 weeks of male C57BL/6 mice (average weight approximately 20 g) were employed to imitate the pathological process of IPF by intranasal injection of 5 mg/kg bleomycin three times. Meanwhile, the control group received intranasal injections of an equivalent volume of PBS. On the fifth day following nasal instillation, one million mouse

https://doi.org/10.1021/acsnano.3c09852
ACS Nano 2024, 18, 5358−5373

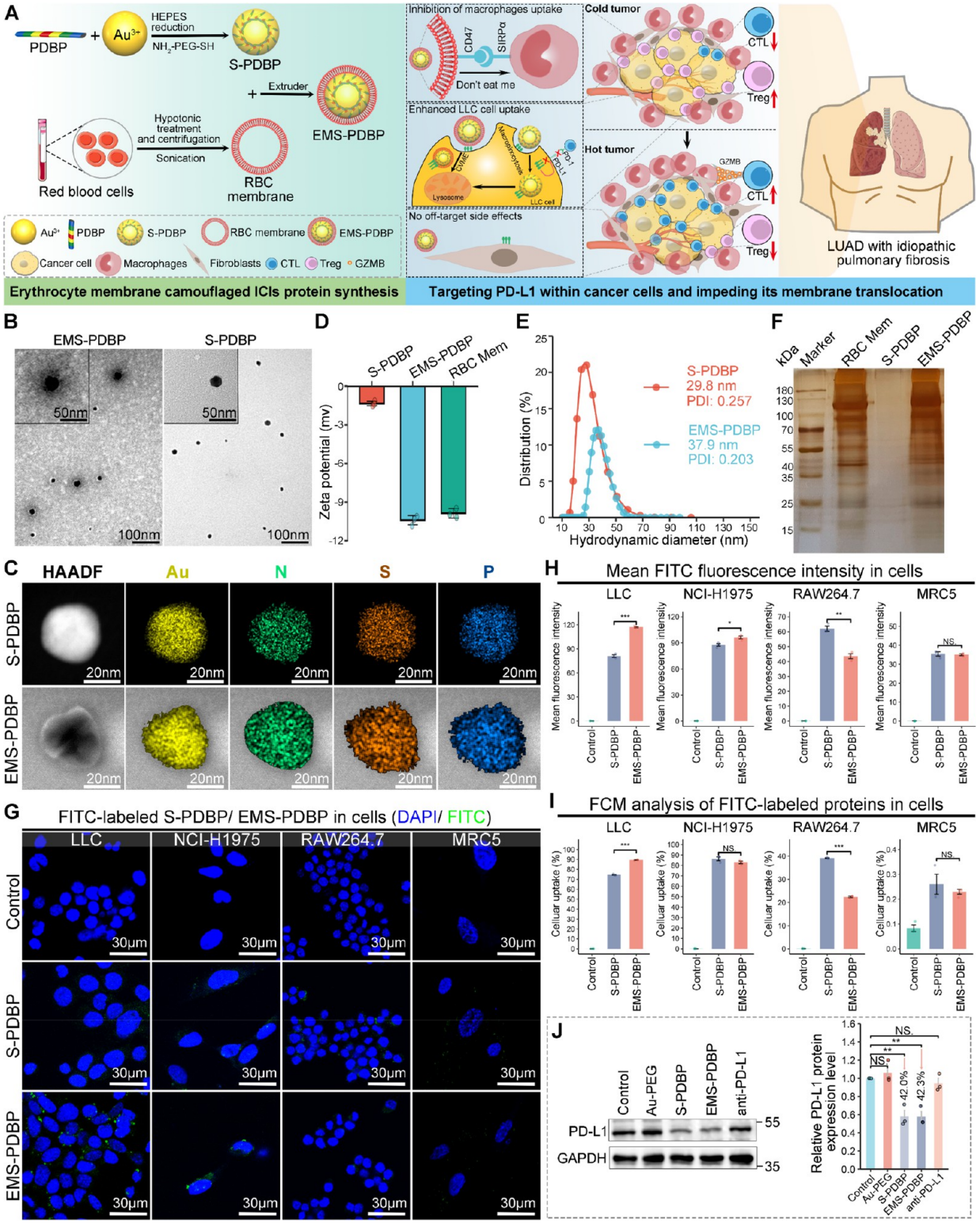

Figure 2. Design and characterization of a biomimetic ICIs protein EMS-PDBP. (A) Schematic illustration of the synthesis and function of EMS-PDBP. (B) Transmission electron microscopy (TEM) images of EMS-PDBP and S-PDBP. (C) High-resolution TEM and overlay elemental analysis images of S-PDBP and EMS-PDBP. (D) Zeta potential of EMS-PDBP, S-PDBP, and erythrocyte membrane (n = 3, mean ± SD). (E) Hydrodynamic diameters of S-PDBP and EMS-PDBP. (F) Protein blots of the erythrocyte membrane, S-PDBP, and EMS-PDBP detected by sodium salt−polyacrylamide gel electrophoresis (SDS-PAGE) with silver-stained. (G) Representative confocal images of lung adenocarcinoma (LUAD) cell lines (NCI-H1975 and LLC), murine macrophage cell line (RAW264.7), and human embryonic lung fibroblast cell line (MRC5) incubated with FITC-labeled S-PDBP and EMS-PDBP for 6 h (n = 3, mean ± SD). (H) Fluorescent intensity analysis of fluorescein isothiocyanate (FITC) in cells with indicated treatments (n = 3, mean ± SD). (I) Statistical analysis of the proportion of FITC-positive cells based on single-channel flow cytometry (n = 3, mean ± SD). (J) Western blot analysis for the expression of PD-L1 in the LLC cell line treated with EMS-PDBP. *P < 0.05; **P < 0.01; ***P < 0.001; NS. Not significant.

https://doi.org/10.1021/acsnano.3c09852
ACS Nano 2024, 18, 5358−5373

LUAD cells, specifically Lewis lung carcinoma cells (LLC), were intravenously incubated into the tail vein of two groups of mice to establish the LC and LC-PF models. Afterward, five successive cycles of anti-PD-1 monoclonal antibody (mAb) at 3 mg/kg were intravenously administered to the mice every other day. The mice were euthanized 5 days following the final intervention, and lung tissue as well as blood samples were collected. The process of modeling and intervention is meticulously outlined in the flowchart (Figure 1D). Ultimately, apparent fibrotic pathological change was observed in the LC-PF model after bleomycin exposure, as evidenced by hematoxylin-eosin (H&E) staining (Figure S2A and Figure S3A), Masson staining (Figure S2B, Figure S3B, and Figure S4A,B), and Sirius red staining (Figure S2C, Figure S3C, and Figure S4C,D) of the lung tissue. The significantly elevated pulmonary index (Figure S5A) and Ashcroft scores (Figure S5B) in the LC-PF group also supported this phenomenon. To confirm the successful reconstruction of the IPF model, the hydroxyproline content of the lung was quantified, and the expression level of fibrotic markers α-SMA and collagen I were evaluated by immunohistochemistry (IHC). Not surprisingly, the LC-PF group yielded higher hydroxyproline content (Figure S5C) and upregulated expression level of collagen I (Figure S6A,B) and α-SMA (Figure S6C,D) in comparison to the LC group. Therefore, the LC-PF model was successfully constructed to simulate the pathological process of lung cancer with coexistent IPF.

The mice in the LC-PF model exhibited significantly heightened levels of inflammatory cell infiltration and severe fibrosis in lung sections compared to those in the LC model following anti-PD-1 mAb treatment (Figure 1E). Reaffirming this observation, the introduction of anti-PD-1 mAb resulted in an apparent surge in leukocyte, neutrophil, and lymphocyte counts within the peripheral blood of mice from the LC-PF group in comparison to the control group (Figure 1F). These results suggested that mice in the LC-PF group exhibited a heightened pulmonary inflammatory response following anti-PD-1 mAb therapy. To delve into the underlying mechanisms of pulmonary inflammation in mice after anti-PD-1 mAb treatment, we conducted RNA-sequencing (RNA-*seq*) analysis of the normal lung tissue from mice. The comparison between the LC-PF and LC groups revealed a total of 428 differentially expressed genes (DEGs), consisting of 327 up-regulated genes and 101 downregulated genes (Figure 1G, H). Employing the mMCP-counter algorithm, we evaluated the composition of 16 immune and stromal cell types within lung tissues derived from both LC-PF and LC mice.[32] The findings unveiled substantially increased levels of infiltrating T cells, $CD8^+$ T cells, macrophages, neutrophils, eosinophils, and fibroblasts in the lung sample of LC-PF mice when contrasted with those in the LC group (Figure 1I). We further investigated the significantly altered biological processes within the lung tissues of mice after anti-PD-1 mAb intervention through gene set enrichment analysis (GSEA). The results indicated that anti-PD-1 mAb intervention activated various biological processes associated with proinflammatory cytokine production in the lung tissues of LC-PF mice, as well as the initiation of the inflammatory response process (Figure 1J). In parallel, we assessed protein expression levels of IL-6 and TNF-α in the lung tissues from both groups of mice using IHC. In alignment with the results of GSEA, our findings revealed a notable augmentation of IL-6 and TNF-α expression levels in the lung tissues of the LC-PF group mice following anti-PD-1 mAb intervention (Figure 1K,L). Furthermore, we noticed that the infiltration level of $CD3^+/CD8^+$ T lymphocytes increased in the lung section of the LC-PF mice after anti-PD-1 mAb intervention via immunofluorescence (IF) staining (Figure 1M). Interestingly, we observed a significantly elevated expression level of PD-L1 in the pulmonary mesenchyme of mice in the LC-PF group compared with the LC group (Figure 1N). Our collective findings suggest that intervention with anti-PD-1 mAb resulted in an excessive activation of T cells and a heightened infiltrating level of diverse inflammatory cells in the pulmonary mesenchyme of mice from the LC-PF group, leading to an escalated production of proinflammatory cytokines IL-6 and TNF-α, consequently exacerbating the pulmonary inflammatory response and resulting in CIP. Therefore, it was postulated that precise targeting of neoplastic PD-L1 exclusively within the tumor microenvironment (TME), while circumventing disruption of the PD-1/PD-L1 axis in extratumoral regions, may effectively eradicate this excessive immune activation in pulmonary mesenchyme.

The Design and Characterization of a Biomimetic ICIs Protein EMS-PDBP. To test this hypothesis and benefit the LUAD patient with coexistent IPF from ICIs, a biomimetic ICIs protein called EMS-PDBP was designed ingeniously with the aim of specifically targeting PD-L1 within tumor cells. The EMS-PDBP is exquisitely crafted through the aurophilicity-driven self-assembly of PDBP peptide, followed by its elegant encapsulation within EM (Figure 2A). The EM encapsulation, according to our design, possesses the capability to modulate the internalization propensity of this engineered ICIs protein toward caveolae-mediated cellular endocytosis.[27] Subsequently, the PDBP peptide would be liberated within intracellular tumors and execute its biofunction by interacting with PD-L1 and sequestering it in the cytoplasm (Figure 2A). The outcome would be the accurate downregulation of PD-L1 abundance on tumor cell surfaces by EMS-PDBP, thereby selectively triggering an immune response against the tumor (Figure 2A). For the preparation of EMS-PDBP, the supramolecular PDBP (S-PDBP) was initially constructed through an aurophilicity-driven self-assembly of the PDBP peptide as described in our previous publication.[22−25,33,34] S-PDBP was successfully self-assembled and connected by the Au−S bond, which was further corroborated by the characterized absorptance peaks of peptide and Au−S bonds in Fourier Transform Infrared (FT-IR) spectroscopy analysis (Figure S7). The reverse-phase high-performance liquid chromatography (HPLC) also showed a satisfactory loading efficiency of 84.5% for S-PDBP (Figure S8). Next, the transparent EM solution was blended with the S-PDBP solution and self-assembled by passing the mixture through a liposome extruder equipped with 200 and 50 nm filters.[35] Of note, the EM, extracted from the red blood cells (RBCs) of healthy C57BL/6 mice, was obtained through a low-osmotic centrifugation method and ultrasonication. Transmission electron microscopy (TEM) revealed a visible membranous structure on the surface of the EMS-PDBP nanoparticle (Figure 2B). Utilizing high-resolution TEM (HRTEM) with a high-angle annular dark-field detector (HAADF) for single-particle imaging, we discerned that the thickness of this membranous structure was approximately 10 nm (Figure 2C), consistent with the reported thickness of EM.[36] Additionally, the superimposed elemental chart and HRTEM images demonstrated a homogeneous dispersion of gold (Au), nitrogen (N), sulfur (S), and phosphorus (P) within the

https://doi.org/10.1021/acsnano.3c09852
ACS Nano 2024, 18, 5358−5373

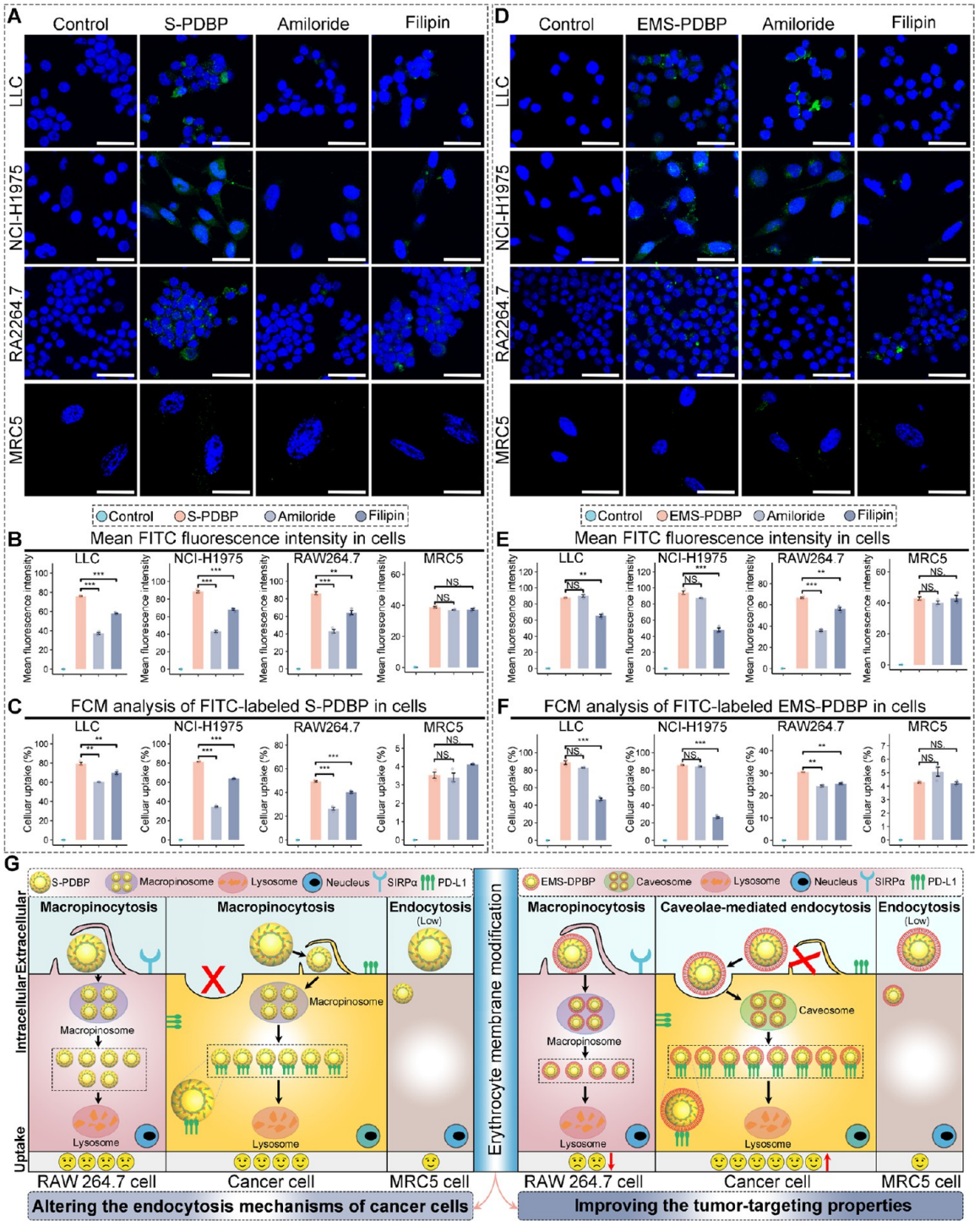

Figure 3. EMS-PDBP exhibited good selectivity in internalizing tumor cells through caveolae-dependent endocytosis. (A) Representative confocal images of lung adenocarcinoma (LUAD) cell lines (NCI-H1975 and LLC), murine macrophage cell line (RAW264.7), and human embryonic lung fibroblast cell line (MRC5) after a 6 h incubation with fluorescein isothiocyanate (FITC)-labeled S-PDBP, either alone or in combination with specific inhibitors. Scale bar: 30 μm. (B) Quantitative analysis of fluorescent intensity from cells treated with indicated conditions (n = 3, mean ± SD). (C) Statistical analysis of the proportion of FITC-positive cells based on single-channel flow cytometry (n = 3, mean ± SD). (D) Representative confocal images of LUAD cell lines (NCI-H1975 and LLC), murine macrophage cell line (RAW264.7), and human embryonic lung fibroblast cell line (MRC5) incubated with either FITC-labeled EMS-PDBP or in combination with indicated inhibitors for 6 h. Scale bar: 30 μm. (E) Fluorescent intensity analysis of FITC in cells with indicated treatment (n = 3, mean ± SD). (F) FITC positive cell proportion statistical analysis based on single channel flow cytometry (n = 3, mean ± SD). (G) Schematic representation illustrating the internalization mechanisms of S-PDBP and EMS-PDBP in both cancer cells and healthy cells. S-PDBP predominantly undergoes internalization in LUAD cells and macrophages via macropinocytosis. After modification with the erythrocyte membrane, EMS-PDBP inhibits macrophage uptake; however, its internalization still relies on macropinocytosis. Notably, the internalization mechanism of EMS-PDBP shifts from macropinocytosis to caveolae-mediated endocytosis in cancer cells. Both S-PDBP and EMS-PDBP show minimal cellular uptake in MRC5 cells. **P < 0.01; ***P < 0.001; NS. Not significant.

https://doi.org/10.1021/acsnano.3c09852
ACS Nano 2024, 18, 5358−5373

nanoparticles (Figure 2C), thus indicating a good uniformity between S-PDBP and EMS-PDBP. In addition, immunogold TEM was utilized to confirm the boundary site of EM on the surface of S-PDBP, suggesting that S-PDBP was connected with the internal membrane of the EM (Figure S9). The Zeta potential of S-PDBP underwent a transition from −1.35 mV to −10.4 mV after EM camouflaging (Figure 2D), which is almost the same as the Zeta potential of EM (−9.8 mV) detected both in this study and another publication.[35] Meanwhile, the hydrodynamic diameter of S-PDBP increased from 29.8 to 37.9 nm upon wrapping with the EM (Figure 2E). Silver staining after sodium salt−polyacrylamide gel electrophoresis (SDS-PAGE) was performed to confirm that the coated monolayer membrane structure is an EM, as evidenced by their similar protein blots (Figure 2F). Collectively, these findings elucidated the successful development of the biomimetic supramolecular termed EMS-PDBP.

The EMS-PDBP Is Selectively Internalized into Tumor Cells, Effectively Leading to the Downregulation of PD-L1 Abundance on the Tumor Cell Membrane. EM camouflage enables nanodrugs to evade uptake by macrophages, thereby enhancing their tumor-targeting accumulation.[37] We verified this phenomenon by comparing the cellular uptake levels of N-terminally fluorescein isothiocyanate (FITC)-labeled S-PDBP and EMS-PDBP in different cell lines. As expected, EM disguise endowed higher cellular uptake levels of FITC-labeled EMS-PDBP in NCI-H1975 and LLC cell lines, suggesting a satisfied tumor cell specificity in LUAD (Figure 2G−I). Conversely, the uptake of EMS-PDBP by macrophages was significantly diminished after EM camouflaging as compared to S-PDBP (Figure 2G−I). To demonstrate that EMS-PDBP was specifically uptake by cancer cells rather than lung fibroblasts in LUAD with coexistent IPF, we conducted further investigations into the cellular uptake of FITC-labeled S-PDBP and EMS-PDBP utilizing the human embryonic lung fibroblast cell line MRC5. Consistent with our expectations, the MRC5 cell line exhibited minimal uptake capacity for both S-PDBP and EMS-PDBP (Figure 2G−I), providing safety assurance for immunotherapy in LUAD patients with coexistent IPF.

To gain a more comprehensive understanding of the cellular uptake of nanoparticles within the *in vitro* inflammatory milieu induced by IPF, cells were pretreated to a concentration of 10 ng/mL recombinant IL-6 for 4 h. Subsequently, FITC-labeled S-PDBP and EMS-PDBP were incubated with the aforementioned cells. Not surprisingly, while IL-6 stimulation slightly increased the cellular uptake of FITC-labeled S-PDBP and EMS-PDBP in both LUAD cancer cell lines and normal cell lines, EMS-PDBP exhibited a specific uptake by LUAD cell lines rather than macrophages and lung fibroblasts (Figure S10). Furthermore, for a precise investigation of the tumor cell targeting ability of EMS-PDBP both *in vitro* and *in vivo*, we quantified the cellular uptake levels of FITC-labeled nanoparticles using a multicellular coculture system and a LC-PF murine model via fluorescence-activated cell sorting (FACS) technology. As expected, EMS-PDBP yielded a satisfactory tumor targeting ability compared to S-PDBP in both *in vitro* (Figure S11) and *in vivo* (Figure S12) cellular uptake studies. Cellular uptake results demonstrated that EMS-PDBP exhibited satisfactory selectivity for cancer cells after EM disguise, indicating a robust tumor-targeting capability *in vivo*. Consequently, we quantified the accumulation of ^{197}Au in the heart, liver, spleen, tumor-bearing lung, and kidney in the LC-PF murine model through inductively coupled plasma mass spectrometry (ICP-MS) after tail vein injection of 2 mg/kg EMS-PDBP or S-PDBP 12 h. As anticipated, EMS-PDBP showed a significantly higher injection dose percentage in the tumor-bearing lung than that of S-PDBP (Figure S13A). Conversely, EMS-PDBP exhibited a significantly lower injection dose percentage in the reticuloendothelial system (RES), including the liver and spleen (Figure S13A). The quantification of organ-specific differential accumulation further highlights the heightened selectivity in the accumulation of EMS-PDBP specifically in the lung affected by tumors (Figure S13B). Overall, these findings indicate that EM modification endows EMS-PDBP with reduced macrophage uptake, satisfactory selectivity for cancer cells, and an effective tumor-targeting capacity.

Next, we verified the selective tumor cell PD-L1 inhibition ability of EMS-PDBP *in vitro*. The abundance of PD-L1 on the tumor cell membrane in LLC (Figure 2J) and NCI-H1975 (Figure S14) cell lines was significantly reduced after 12 h of incubation at a concentration of 100 nM with EMS-PDBP, confirming our expectations compared to the other groups. These results revealed that EMS-PDBP could be specifically uptaken by LUAD cell lines, showcasing its satisfied tumor-targeting capability. Furthermore, EMS-PDBP exhibits good precision and efficiency in diminishing the abundance of PD-L1 protein on the cellular membrane of LUAD cells, thus positioning it as a promising and innovative nanomedicine for immunotherapy.

EMS-PDBP Exhibited Good Selectivity in Internalizing Tumor Cells through Caveolae-Dependent Endocytosis. Cellular uptake experiments unequivocally showcased the satisfied tumor targeting ability of EMS-PDBP to LUAD cell lines, with no discernible off-target repercussions noted in the MRC5 cell line, even in the presence of IL-6 stimulation. The internalization level of EMS-PDBP in the LLC cell line significantly increased after being enveloped by EM, as observed. These results suggested that EM disguise may have instigated an alteration in the supramolecular internalization mechanism.[27] To verify this, we investigated the internalization pathways of S-PDBP and EMS-PDBP in different cell lines. We initially pretreated the cell lines with amiloride (a macropinocytosis inhibitor) and filipin (a caveolae-dependent endocytosis inhibitor) for 1 h, followed by incubation with FITC-labeled S-PDBP for 6 h. In the presence of amiloride and filipin, a noteworthy decrease in the level of cellular uptake of S-PDBP was noted across the LLC, NCI-H1975, and RAW264.7 cell lines (Figure 3A−C). Importantly, the inhibitory impact of amiloride surpassed that of filipin, indicating that the internalization of S-PDBP into these cells predominantly occurred through macropinocytosis. Subsequently, we delved into the impact of EM modification on the internalization mechanism of EMS-PDBP. Surprisingly, we observed that amiloride failed to impede the uptake of EMS-PDBP in both LLC and NCI-H1975 cell lines (Figure 3D−F). Conversely, filipin considerably hindered the uptake of EMS-PDBP in these cell lines (Figure 3D−F). These observations point to a shift in the cellular internalization mechanism of EMS-PDBP in LUAD cell lines after EM camouflaging, transitioning from macropinocytosis to caveolin-mediated endocytosis.[27] Moreover, we identified that the internalization mechanism of macrophages continues to depend on macropinocytosis, even after EM encapsulation (Figure 3A−F). Both S-PDBP and EMS-PDBP displayed limited internalization

https://doi.org/10.1021/acsnano.3c09852
ACS Nano 2024, 18, 5358−5373

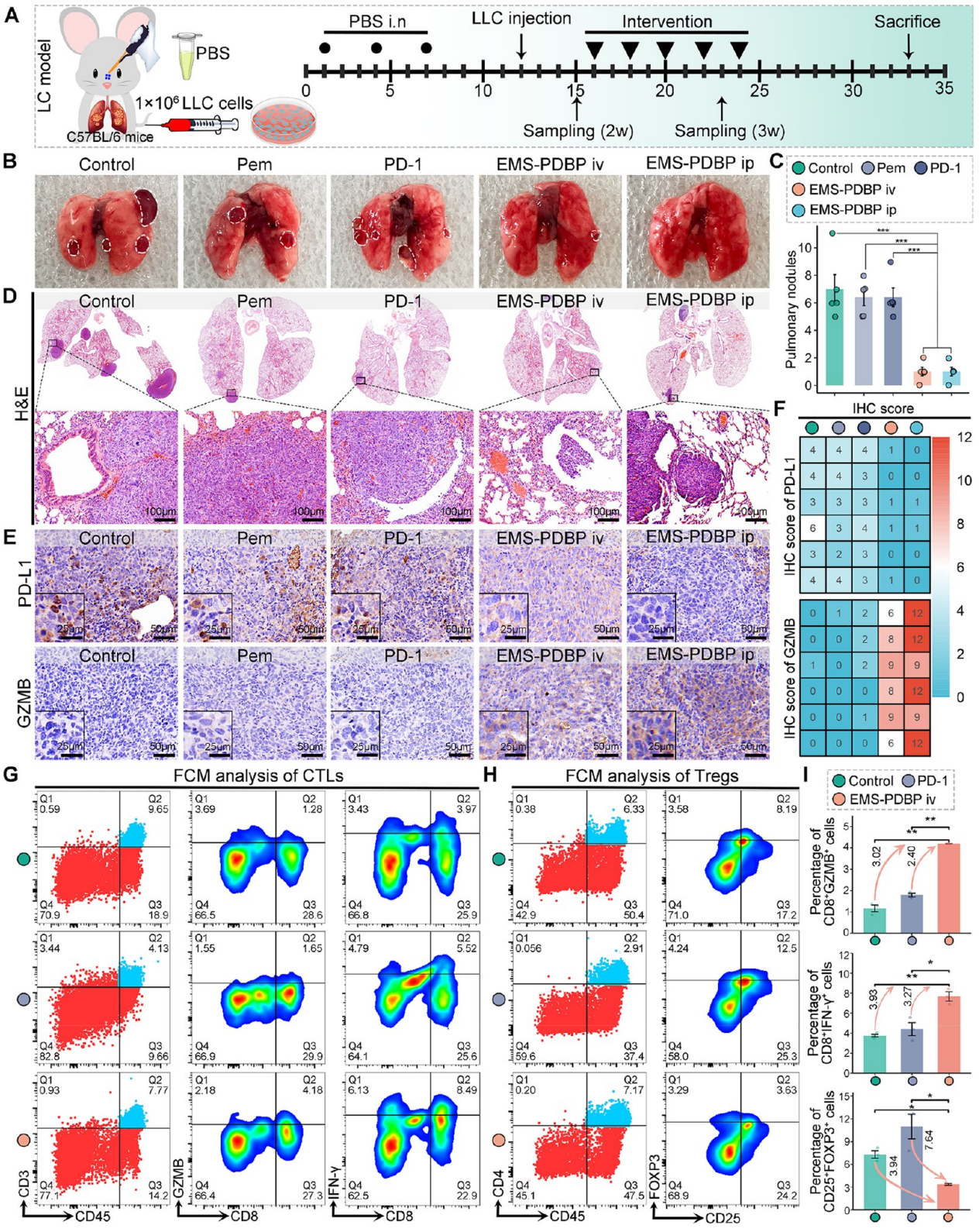

Figure 4. EMS-PDBP augmented antitumor immunotherapy in an orthotopic murine model of LUAD *in vivo*. (A) Schematic representation illustrating the establishment and intervention of the lung adenocarcinoma (LUAD) orthotopic murine model. (B–D) Representative photograph (B), comparison of nodule counts (C), and representative H&E images (D) of mouse lungs under different treatments. (E,F) Representative immunohistochemistry (IHC) staining images (E) and heatmap depicting IHC scores (F) for PD-L1 and Granzyme B (GZMB) in the indicated treatment groups (n = 6, mean ± SD). (G,H) Representative flow cytometry diagrams showing the proportions of cytotoxic lymphocytes (CTLs) (G) and regulatory T cells (Tregs) (H) in the lung tumor from mice with the indicated treatments. (I) Quantification analysis of $CD8^+GZMB^+$, $CD8^+IFN\text{-}\gamma^+$, and $CD25^+FOXP3^+$ cells in the lung tumors (n = 3, mean ± SD). *P < 0.05; **P < 0.01; ***P < 0.001.

https://doi.org/10.1021/acsnano.3c09852
ACS Nano 2024, 18, 5358–5373

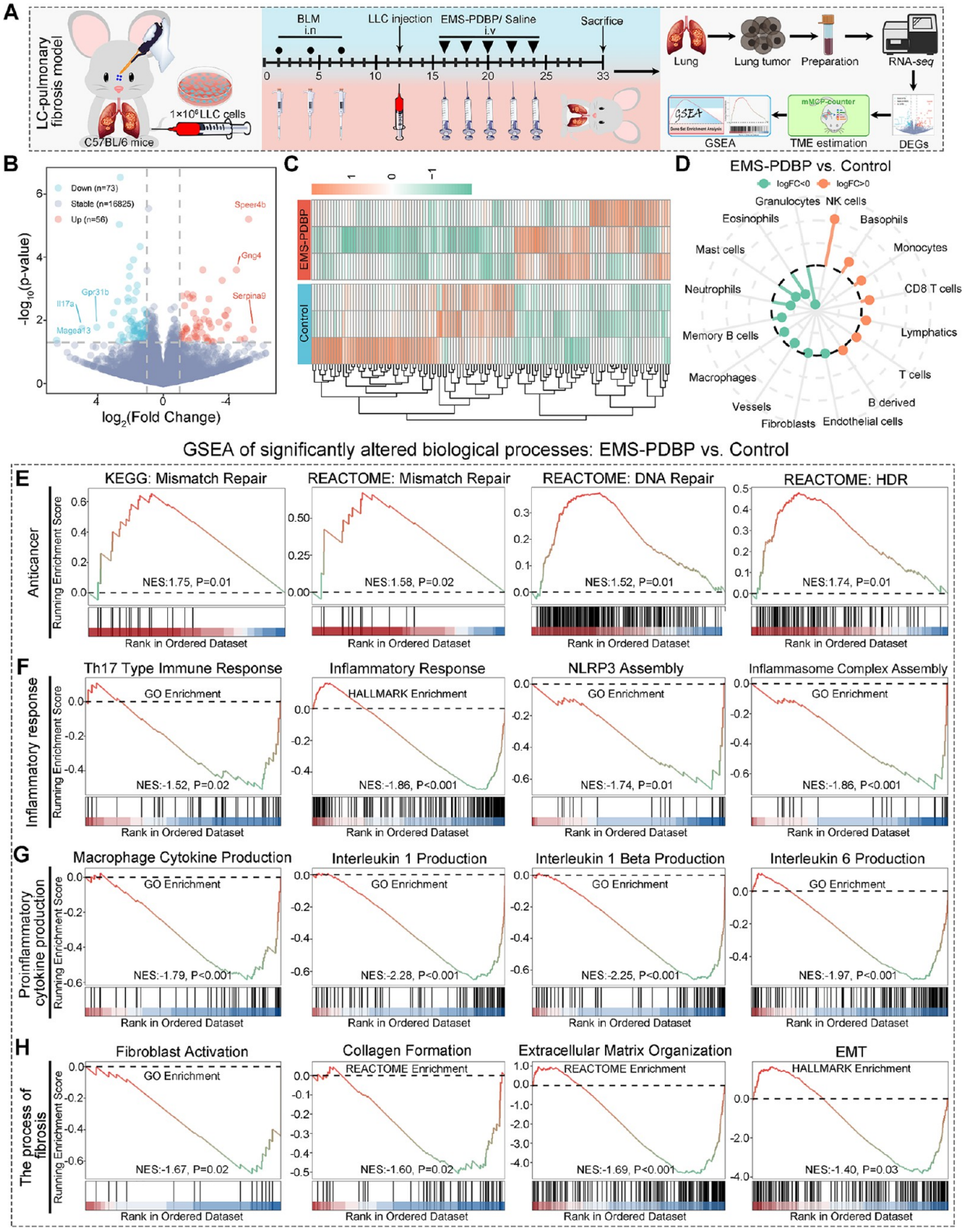

Figure 5. ***In vivo*** **antitumor mechanism of EMS-PDBP in the orthotopic LUAD murine model with coexistent IPF. (A) The flow diagram illustrating the establishment and intervention of the lung adenocarcinoma (LUAD) tumor-bearing idiopathic pulmonary fibrosis model. (B,C) Volcano plot showing the differentially expressed genes (DEGs) (B) and hierarchical clustering heatmap revealing gene expression patterns (C) in the lung tumor after EMS-PDBP and saline treatment. (D) Ranking plot displaying alterations in infiltration of 16 types of immune and stromal cells within mouse lung tumors, as estimated by the mMCP-counter algorithm following the indicated treatments. (E–H) Gene set enrichment analysis (GSEA) analysis highlighting the significantly altered pathways in the lung tumor after EMS-PDBP treatment, involving antitumor related pathways (E), inflammatory response related pathways (F), proinflammatory cytokine production related pathways (G), and fibrosis related pathways (H).**

https://doi.org/10.1021/acsnano.3c09852
ACS Nano 2024, 18, 5358−5373

within the MRC5 cell line, and there was no significant uptake change, even with amiloride and filipin intervention (Figure 3A−F). Consistent results were observed even when the cells mentioned above were pretreated with 10 ng/mL IL-6 for 4 h to simulate the inflammatory environment induced by IPF *in vitro* (Figure S15). These results collectively implied that caveolin-dependent endocytosis is pivotal in mediating the internalization of EMS-PDBP, facilitating an improved targeting efficiency and enhanced accumulation within cancer cells (Figure 3G).

The Administration of EMS-PDBP Resulted in a Reduction in the Abundance of PD-L1 and Facilitated the Infiltration of CTLs in an Orthotopic Murine Model of LUAD. In recent decades, ICB has completely changed the treatment landscape of LUAD. National Comprehensive Cancer Network (NCCN) guidelines have provided a moderate recommendation for Pembrolizumab, a PD-1 neutralizing mAb, as either first-line or standalone treatment for LUAD immunotherapy.[9,10] Here, EMS-PDBP was introduced into the previously mentioned LC murine model to challenge the efficacy and safety of conventional LUAD therapeutic drugs. Despite intranasal administration providing superior pulmonary targeting, we chose not to proceed due to the mice's prior receipt of three intranasal injections of bleomycin or PBS. Administering an additional five intranasal injections of antitumor drugs in this context would worsen pulmonary side effects. Therefore, all mice were allocated randomly into the following treatment groups and followed by five successive intravenous injections of normal saline (control, every other day), Au-PEG (2 mg/kg, once daily), Pemetrexed (Pem 3 mg/kg, every other day), anti-PD-1 mAb (PD-1 3 mg/kg, every other day), S-PDBP (2 mg/kg, once daily), EMS-PDBP (2 mg/kg, once daily), and intraperitoneal injection of EMS-PDBP (3 mg/kg, every other day). The mice were ultimately euthanized, and their blood samples, lungs, and other organs were subsequently collected for further analysis (Figure 4A). Excitingly, both intravenous and intraperitoneal administration of EMS-PDBP yielded a significant reduction in pulmonary nodules (Figure 4B,C and Figure S16) as well as tumor foci (Figure 4D and Figure S16), in stark comparison to other treatment groups. Consistent with the *in vitro* study, EMS-PDBP could significantly decrease the PD-L1 expression level in tumor cells *in vivo*, as evidenced by the IHC images of lung tumor sections (Figure 4E,F). Additionally, the expression level of Granzyme B (GZMB) within lung tumor sections was up-regulated after EMS-PDBP intervention (Figure 4E,F), thereby indicating a heightened antitumor immune response driven by T cells. Therefore, we investigated the infiltration level of cytotoxic T lymphocytes (CTLs) and regulatory T cells (Tregs) within the tumors through FACS and IF staining. As expected, EMS-PDBP enhanced the infiltration density of CTLs (Figure 4G,I, Figure S17, and Figure S19A) at the tumor sites. In contrast, the infiltration level of Tregs (Figure 4H,I, Figure S18, and Figure S19B) in the tumor was significantly diminished after EMS-PDBP administration.

Combining the PD-L1 inhibition ability of EMS-PDBP *in vivo*, these results elucidated that EMS-PDBP could enhance antitumor immunotherapy by recovering the killing effect of CTLs in the TME through the effective inhibition of PD-L1 in tumor cells. Furthermore, the administration of EMS-PDBP did not result in a substantial alteration in the body weight of these mice (Figure S20A). Next, we evaluated the pulmonary toxicity at the end of drug administration to demonstrate that EMS-PDBP could ameliorate the occurrence of pulmonary side effects of anti-PD-1 mAb therapy. Not surprisingly, EMS-PDBP did not result in pneumonia, as evidenced by the normal histopathological findings observed in the lung sections stained with H&E (Figure S20B). Conversely, administration of the anti-PD-1 mAb induced notable pulmonary inflammation, characterized by heightened infiltration of inflammatory cells within the lung sections (Figure S20B). Consistent with the above results, the expression levels of IL-6 and TNF-α in both lung tissues and serum of LC mice were significantly increased following anti-PD-1 mAb intervention compared with the other groups (Figure S20C−E and Figure S21A,B). However, it is worth noting that EMS-PDBP did not contribute to an elevation in the expression levels of these cytokines (Figure S20C−E and Figure S21A,B). EMS-PDBP intervention also exhibited a commendable profile of hematological safety, as demonstrated by stable levels of hemoglobin, platelets, erythrocytes, and leukocytes (Figure S22A). In addition, after five cycles of EMS-PDBP intervention, there were no abnormal changes observed in the levels of albumin (ALB), total bilirubin (TBIL), alanine aminotransferase (ALT), aspartate aminotransferase (AST), blood urea nitrogen (BUN), or creatinine (CREA) (Figure S22B). Besides, the liver (Figure S22C) and kidney (Figure S22D) slices had no abnormal pathological damage, underscoring the favorable hepatic and nephrotic safety profiles of EMS-PDBP. Moreover, the heart (Figure S23) and spleen (Figure S24) pathological sections further corroborated the excellent biocompatibility of EMS-PDBP. Taken together, the therapeutic supramolecular EMS-PDBP is sufficiently safe to aid the immunotherapy efficacy of LUAD by inhibiting the suppressive TME and awaking normal antitumor immunity of CTLs through downregulating the PD-L1 in tumor cells.

The Administration of EMS-PDBP Avoided the Inflammatory Response in the Pulmonary Mesenchyme in the Orthotopic LUAD Murine Model with Coexistent IPF, while Maintaining a Favorable Safety Profile. Given that EMS-PDBP has strong antitumor immunity in the LC mice model. Besides, the *in vitro* study revealed that lung fibroblasts hardly uptake EMS-PDBP. Could EMS-PDBP serve as a potential immunotherapeutic agent for LUAD with coexistent IPF? Therefore, we first utilized the previously mentioned LC-PF model to explore the potential antitumor mechanisms of EMS-PDBP in LUAD with coexistent IPF. Lung tumor samples were collected for RNA-*seq* analysis after five successive dosages of EMS-PDBP intravenous injection (2 mg/kg, once daily) (Figure 5A). Overall, a total of 129 DEGs were identified between the EMS-PDBP and control groups, with 56 genes being up-regulated and 73 genes being downregulated (Figure 5B,C). After applying the mMCP-counter algorithm for the quantification of immune and stromal cells in tumor tissues, we observed significantly higher levels of infiltrated NK cells, $CD8^+$ T cells, and T cells in the lung tumor tissues after EMS-PDBP intervention (Figure 5D). This observation implied that EMS-PDBP could potentiate the antitumor immune response in LC-PF mice. GSEA unveiled the association of EMS-PDBP intervention with the activation of diverse pathways pertinent to antitumor responses, encompassing mismatch repair, DNA repair, and homology-directed repair (HDR) (Figure 5E). Furthermore, GSEA also exhibited that EMS-PDBP could significantly inhibit biological processes related to the inflammatory response (Figure 5F), proinflammatory cytokine production (Figure 5G), and fibrosis

https://doi.org/10.1021/acsnano.3c09852
ACS Nano 2024, 18, 5358−5373

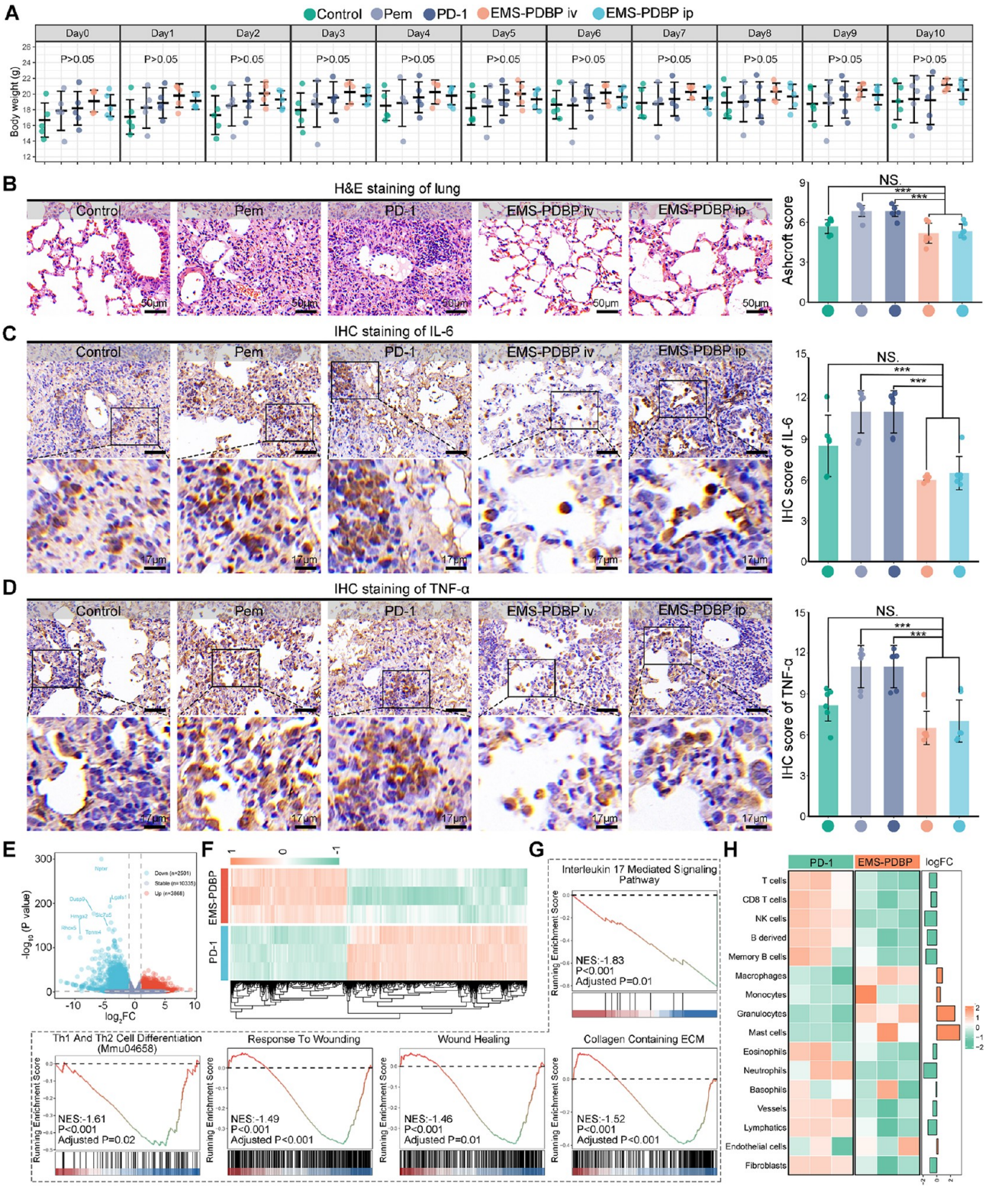

Figure 6. EMS-PDBP mitigated the occurrence of CIP through inhibiting the inflammatory response in the orthotopic LUAD murine model with coexistent IPF. (A) The body weight change of each mouse with indicated intervention (n = 5, mean ± SD). (B) Representative H&E staining images and Ashcroft scores of lungs in the indicated treatment groups (n = 6, mean ± SD). (C,D) Representative immunohistochemistry (IHC) staining and corresponding IHC score of IL-6 (C) and TNF-α (D) in the lung tissue from the indicated treatments (n = 6, mean ± SD). Scale bar of the upper panel: 50 μm. (E,F) Volcano plot (E) and hierarchical clustering heatmap (F) illustrating the differentially expressed genes (DEGs) in the normal lung tissue from mice treated with EMS-PDBP and anti-PD-1 mAb. (G) Gene set enrichment analysis (GSEA) showcasing the significantly inhibited biological processes in the lung tissue of mice after EMS-PDBP treatment, involving the inflammatory response and fibrosis related pathways. (H) Heatmap displaying the infiltration of 16 immune and stromal cell types, estimated using the mMCP-counter algorithm across different experimental groups. Infiltration values were normalized, and Log (fold change) of immune and stromal cells was calculated to reflect their alterations. ***P < 0.001; NS. Not significant.

https://doi.org/10.1021/acsnano.3c09852
ACS Nano 2024, 18, 5358−5373

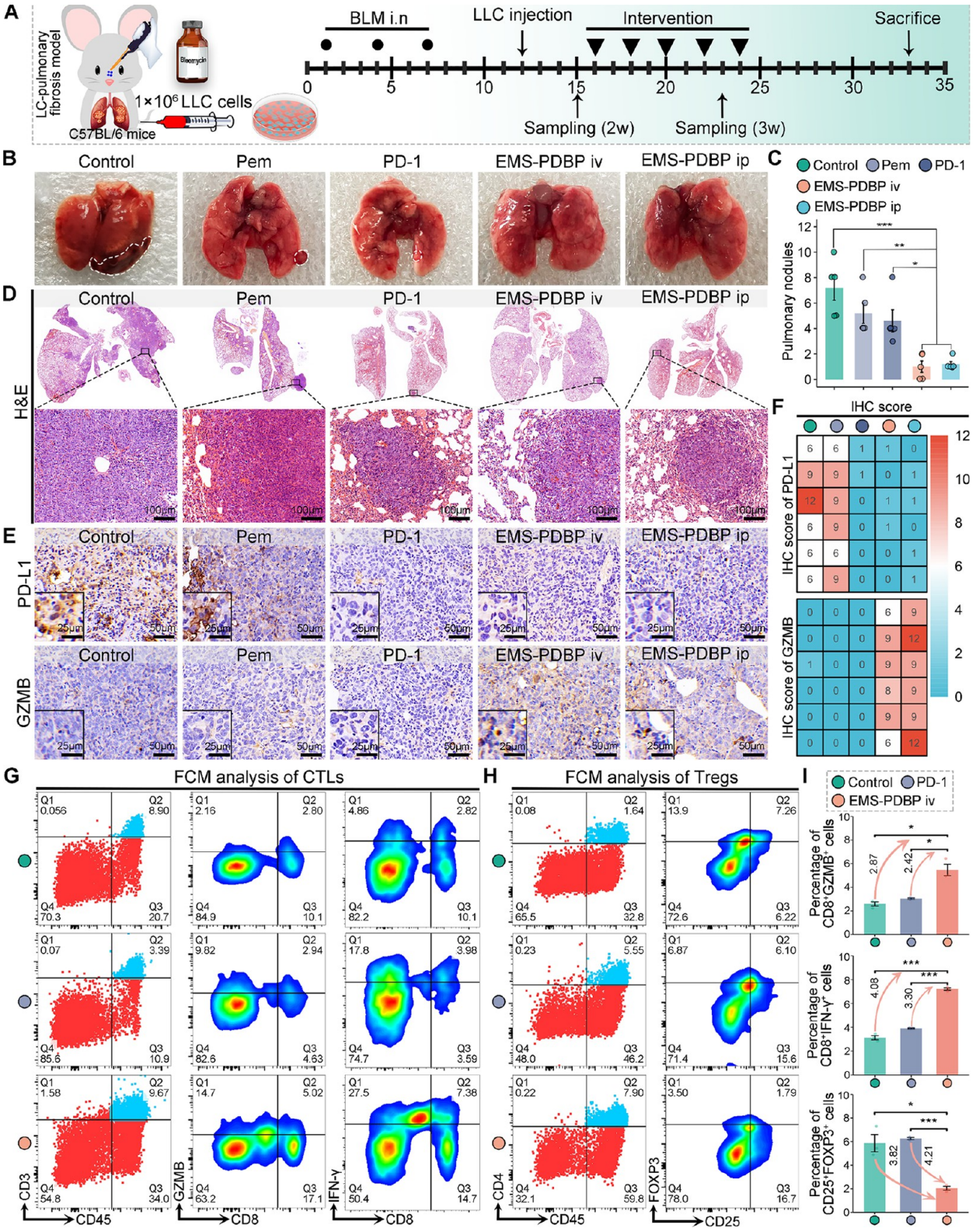

Figure 7. Antitumor immunotherapy efficacy of EMS-PDBP in a murine model of orthotopic LUAD with coexistent IPF. (A) Diagram illustrating the construction and intervention of the lung adenocarcinoma (LUAD) tumor-bearing idiopathic pulmonary fibrosis murine model. (B–D) Representative photograph (B), comparison of nodule counts (C), and representative H&E images (D) of lung sections from mice subjected to the designated treatments (n = 5, mean ± SD). (E,F) Representative immunohistochemistry (IHC) staining images (E) and heatmap depicting IHC scores (F) for PD-L1 and Granzyme B (GZMB) in the indicated treatment groups (n = 6, mean ± SD). (G,H) Representative flow cytometry diagrams showing the proportions of cytotoxic lymphocytes (CTLs) (G) and regulatory T cells (Tregs) (H) in the lung tumor from mice with the indicated treatments. (I) Quantification analysis of $CD8^+GZMB^+$, $CD8^+IFN\text{-}\gamma^+$, and $CD25^+FOXP3^+$ cells in the lung tumor (n = 3, mean ± SD). *P < 0.05; **P < 0.01; ***P < 0.001.

https://doi.org/10.1021/acsnano.3c09852
ACS Nano 2024, 18, 5358–5373

(Figure 5H). In summary, EMS-PDBP holds promise as a secure and efficacious immunotherapeutic nanomedicine for LC-PF mice.

Next, we meticulously investigated the safety profile of EMS-PDBP in LC-PF mice in comparison to other commonly utilized therapeutic drugs for LUAD. Not surprisingly, EMS-PDBP did not exert a noteworthy impact on the body weight of mice throughout the treatment cycle (Figure 6A). It is worth noting that histological examination of lung sections through H&E staining demonstrated that EMS-PDBP did not escalate pulmonary inflammatory response or fibrosis severity in the mice (Figure 6B). Nonetheless, the administration of anti-PD-1 mAb resulted in a pronounced pulmonary inflammatory response (Figure 6B), suggesting that EMS-PDBP would not increase the likelihood of CIP occurrence in LUAD with coexistent IPF. We subsequently compared the protein expression levels of IL-6 and TNF-α in both lung tissue and serum samples from mice subjected to various treatment regimens. Consistently, the EMS-PDBP group showed no significant increase in IL-6 (Figure 6C and Figure S25A) and TNF-α (Figure 6D and Figure S25B) expression in the lung tissues and serum, while anti-PD-1 mAb intervention significantly increased their expression levels (Figure 6C,D). The hematological safety profile illustrated that EMS-PDBP intervention maintained stable leukocyte, neutrophil, and lymphocyte counts in the peripheral blood of mice when compared to other treatment groups (Figure S26A). Besides, serum tests (Figure S26B) and pathological sections of the liver and kidney (Figure S26C) also corroborated the favorable safety profile of EMS-PDBP in these organs. H&E staining of the heart (Figure S27) and spleen (Figure S28) sections also revealed no abnormal pathological changes after EMS-PDBP therapy. Collectively, EMS-PDBP exhibited excellent biocompatibility in LC-PF mice without increasing irAEs, particularly the occurrence of CIP. In contrast, the introduction of anti-PD-1 mAb significantly heightened the risk of CIP in LC-PF mice.

The systemic introduction of anti-PD-1 mAb would promote lymphocyte infiltration into the lungs by inducing an unexpected activation of the immune response, consequently triggering cytokine release syndrome and ultimately resulting in CIP.[38] Subsequently, we delved into the potential mechanisms that could account for the disparity in CIP occurrence between EMS-PDBP and anti-PD-1 mAb in the LC-PF model through RNA-*seq* analysis. In this context, mice were subjected to intravenous doses of anti-PD-1 mAb (3 mg/kg, every other day) and EMS-PDBP (2 mg/kg, once daily) for 5 cycles. Then, normal lung tissues were harvested for the RNA-*seq* analysis. In total, 6369 DEGs were discerned after EMS-PDBP intervention, encompassing 3868 up-regulated genes and 2501 downregulated genes (Figure 6E, F). GSEA indicated that EMS-PDBP significantly inhibited multiple biological processes related to the inflammatory response and fibrosis (Figure 6G). Utilizing mMCP-counter, we unveiled a noticeable reduction in the levels of infiltrating T cells, $CD8^+$ T cells, eosinophils, and neutrophils, all associated with inflammation, within the lung tissues of mice after EMS-PDBP intervention (Figure 6H). Notably, the infiltration of fibroblasts associated with the progression of fibrosis was also substantially diminished (Figure 6H). Collectively, these findings underscored the auspicious biocompatibility of EMS-PDBP in inducing antitumor effects in LC-PF mice. Significantly, they also showcased the potential of EMS-PDBP in reducing the likelihood of CIP incidence by dampening inflammatory responses in healthy lung tissues.

The Administration of EMS-PDBP Effectively Activates the Antitumor Immune Response in a Murine Model of Orthotopic LUAD with Coexistent IPF. Considering the robust antitumor immune response and favorable safety profile exhibited by EMS-PDBP in LC-PF mice, it holds great promise as a viable immunotherapeutic approach for LUAD with coexistent IPF. Hence, we administered EMS-PDBP in the LC-PF murine model to assess its antitumor effects in comparison with other conventional therapeutic drugs. The comprehensive procedures for modeling and intervention are elucidated in Figure 7A. As anticipated, EMS-PDBP intervention significantly reduced the count of pulmonary nodules (Figure 7B,C) and the extent of tumor area in the H&E sections (Figure 7D) compared to the other treatment groups. Consistent with the *in vitro* study and the function of PD-L1 downregulation observed in the LC model, EMS-PDBP also displayed a proficient downregulation of PD-L1 in tumor cells within the LC-PF model (Figure 7E,F). Additionally, a noteworthy escalation in GZMB levels within the lung IHC sections was evident after the administration of EMS-PDBP treatment (Figure 7E,F). Most strikingly, both FACS analysis and IF staining indicated that EMS-PDBP administration can substantially elevate the infiltration levels of CTLs within the lung TME (Figure 7G,I and Figure S29A). Simultaneously, there was a concurrent reduction in the levels of infiltrated Tregs (Figure 7H,J; Figure S29B) in the lung TME of the LC-PF model. Taken together, in the LC-PF murine model, EMS-PDBP is also capable of targeted downregulating PD-L1 in tumor cells, reversing the suppressive TME, boosting the cytotoxicity of CTLs against tumor cells, ultimately leading to a robust antitumor immune response.

CONCLUSION

The coexistence of LUAD and IPF has long been regarded as a confined domain for ICIs, yet recent meta-analysis findings have unveiled a significantly heightened incidence of CIP following ICIs treatment in individuals with lung cancer and preexisting ILD (overall: 27%; severe cases: 15%).[8] Furthermore, a multicenter, single-arm phase 2 trial of anti-PD-L1 Atezolizumab in 2020 that was initiated to evaluate the efficacy in lung cancer patients with ILD had to be prematurely terminated due to the heightened incidence of CIP among the enrolled participants (occurring in 29.4% of cases for all grades and 23.5% for grades $\geq$3).[39,40] A groundbreaking approach was employed in this study to specifically target PD-L1 within the cellular interior, transcending the conventional focus solely on the cytomembrane. This innovative strategy enables the development of ICIs that can discern between LUAD cells and noncancerous cells based on their distinctive endocytic propensities. By harnessing aurophilicity-driven self-assembly PDBP and subsequently encapsulating it within EM, the resulting biomimetic ICIs protein EMS-PDBP exhibits significant selectivity in internalizing cells, effectively targeting PD-L1 within cancer cells while impeding its membrane translocation. The EMS-PDBP treatment not only reactivated the antitumor immune response in the LUAD orthotopic allograft mouse model but also demonstrated a favorable safety profile by effectively eliminating any irAEs. Most significantly, EMS-PDBP successfully and safely restored the antitumor immune response in a mouse model of LUAD with coexistent

https://doi.org/10.1021/acsnano.3c09852
ACS Nano 2024, 18, 5358−5373

IPF, thus shattering the confines of ICIs immunotherapy. The reported EMS-PDBP collectively presents a tumor immunotherapy strategy with clinical translational potential for surmounting the limitations of immunotherapy in LUAD coexisting with IPF. However, given the derivations of the EM in EMS-PDBP, it should be adapted to the human EM when it is applied in humans.

METHODS

Synthesis and Characterization of EMS-PDBP. The bionic supramolecule, EMS-PDBP, was synthesized through aurophilicity-driven self-assembly and the camouflaging of the EM as previously described.[22−25,33,34] Initially, 2 mg of PDBP was dissolved in a solution comprising 500 μL of ethanol and 1.25 mL of ddH_2O. This solution was then combined with an aqueous mixture of tetra chloroauric acid, NH_2-PEG-SH, and HEPES, followed by sonication for 10 min. Excess reagents were removed through dialysis tubing (10 kDa cutoff) and two rinses with distilled water, resulting in the synthesis of S-PDBP. In the subsequent step, a liposome extruder was used to assemble S-PDBP and the EM. The previously prepared EM and S-PDBP were introduced into PBS at a volume ratio of 1:1000. This mixture underwent ultrasonication at 30 W for 5 s, with a 2 s pause, repeated over a 2 min period, and was then allowed to settle on ice for 20 min. Finally, self-assembly was achieved by sequentially passing the mixture through a liposome extruder equipped with 200 and 50 nm filters.[35]

The successful assembly of S-PDBP was confirmed through FT-IR spectroscopy, revealing characteristic absorptance peaks corresponding to the peptide and Au−S bonds. The loading efficiency of S-PDBP was determined using reverse phase HPLC. Morphological features of S-PDBP and EMS-PDBP were examined by TEM and HRTEM, with HRTEM used to assess the spatial distribution of Au, N, S, and P within the nanoparticles. Immunogold TEM was employed to verify the binding site of EM on the surface of S-PDBP, using CD47 and EPB42 as external and internal membrane proteins of EM, respectively.[41−43] In brief, 100 nm AuNPs were labeled with anti-CD47 and anti-EPB42 antibodies for 1 h. Subsequently, EMS-PDBP was incubated with the antibody-labeled AuNPs for 1 h in a 1% BSA water solution. The samples were then applied to a copper grid for TEM analysis. The hydrodynamic size distribution and Zeta potential of S-PDBP and EMS-PDBP were determined by using dynamic light scattering (DLS) measurements. The membrane proteins of EMS-PDBP were characterized by silver staining after SDS-PAGE.

Endocytosis Mechanism of EMS-PDBP. The RAW264.7, NCI-H1975, LLC, and MRC5 cell lines were seeded onto six-well dishes, with or without circular cover glass, and cultured in complete medium until reaching approximately 70% density. Subsequently, the culture medium was replaced with serum-free medium, and cells were pretreated with amiloride (400 μM) and filipin (2 μg/mL) for 1 h. FITC-labeled S-PDBP or EMS-PDBP was then introduced into the medium and used to treat the cells for 6 h. For flow cytometry quantitative analysis, the medium was carefully aspirated and cells were digested. Afterward, the cells were washed three times with ice-cold PBS and resuspended for analysis. For laser confocal scanning microscope analysis, cells were washed three times with ice-cold PBS, fixed at room temperature for 15 min, and then, after three gentle washes with ice-cold PBS, incubated in a DAPI staining solution for 15 min at room temperature. Confocal laser-scanning microscopy was utilized to capture images. Mean fluorescence intensity was calculated using ImageJ for subsequent statistical analysis.

Orthotopic Murine Model of LUAD with or without Coexistent IPF. Animal study was approved by the Animal Ethics Committee of Xi'an Jiaotong University (Approval No: 2022−0059). Currently, the most common approach to replicate the pathological process of human IPF in C57BL/6 mice involves intratracheal injection of the cytotoxic drug bleomycin.[44,45] In our study, 5 mg/kg of bleomycin or an equal amount of PBS was intranasally introduced to male C57BL/6 mice three times. Subsequently, after 5 days of bleomycin or PBS injection, 1×10^6 LLC cells were intravenously inoculated into the mice to establish the orthotopic murine model of LUAD with coexistent IPF (LC-PF) or without (LC). Following the indicated treatments, blood specimens, lungs, and other organs were collected for further analysis. Mouse lung samples were collected, fixed, embedded, and sectioned into 5 μm slices for subsequent H&E staining, Masson's trichrome staining, Sirius red staining, IHC staining, and IF staining. Pulmonary fibrosis severity was evaluated on an Ashcroft scale, scored from 0 to 8.[46] Quantification of Masson's stain and Sirius red stain positive areas was performed using ImageJ. Hydroxyproline levels in the lung tissues were assessed using the mouse hydroxyproline ELISA Kit following a standardized protocol. IHC staining of α-SMA, COL1A1, IL-6, and TNF-α was employed to confirm the successful replication of pulmonary fibrosis. To assess treatment efficacy, pulmonary nodule counting, H&E staining of lung tumors, and IHC staining of GZMB and PD-L1 were conducted. For biosafety evaluation, changes in body weight, blood routine tests, and liver and kidney function were monitored, including hemoglobin, platelets, RBCs, WBCs and their classification, ALB, TBIL, ALT, AST, BUN, and CREA. H&E staining of liver and kidney slices was adopted to assess histological changes after pharmaceutical intervention. Additionally, H&E staining of the heart and spleen was used to evaluate heart and hematological safety profiles. Serum cytokines IL-6 and TNF-α were measured to reflect the systemic inflammatory status of mice after different treatments using commercial ELISA kits as per the instruction manual.

ASSOCIATED CONTENT

Supporting Information

The Supporting Information is available free of charge at https://pubs.acs.org/doi/10.1021/acsnano.3c09852.

The pooled incidence of any grade of CIP in lung cancer patients with and without preexisting ILD; Lung histopathological sections, pulmonary index, Ashcroft scores, hydroxyproline content, and IHC staining of COL1A1 and α-SMA between LC and LC-PF murine models; FT-IR spectroscopy, reverse-phase HPLC, and immunogold TEM of S-PDBP or EMS-PDBP; Cellular uptake levels of FITC-labeled S-PDBP and FITC-labeled EMS-PDBP *in vitro* and *in vivo*; The tumor-targeting ability of EMS-PDBP in the LC-PF murine model; Western blot to depict EMS-PDBP could selectively target PD-L1 in NCI-H1975 cell line; Cellular uptake levels of FITC-labeled S-PDBP and FITC-labeled EMS-PDBP following 4-h stimulation with 10 ng/mL IL-6 and in the presence of the indicated inhibitors; Pulmonary nodules and tumor foci of LC murine model in the indicated treatment groups; The flow cytometry-based representative gating strategy of CTLs and Tregs; Representative IF double staining of CTLs and Tregs in the LC model; Safety evaluation of different treatments in the LC and LC-PF models; Representative IF double staining of CTLs and Tregs in the LC-PF model (Figure S1−S29); Characteristics of the included studies in the Meta-analysis (Table S1); The process of Meta-analysis; Synthesis of PDBP peptide and EM isolation; Synthesis and characterization of EMS-PDBP; Flow cytometry and laser confocal scanning microscope analysis for cellular uptake quantification; Internalization mechanism of nanoparticles study; Western blot; Construction, intervention, and histopathological analysis of LC and LC-PF murine models; Lung tumor flow cytometry; Cellular uptake quantification *in vivo* and lung tumor targeting ability evaluation; RNA-*seq* and tissue-infiltrating

https://doi.org/10.1021/acsnano.3c09852
ACS Nano 2024, 18, 5358−5373

immune and stromal cells estimation; Toxicity studies; Statistical analysis (Supplementary Methods) (PDF)

AUTHOR INFORMATION

Corresponding Authors

Jin Yan − *National & Local Joint Engineering Research Center of Biodiagnosis and Biotherapy, The Second Affiliated Hospital of Xi'an Jiaotong University, Xi'an 710004, China;* orcid.org/0000-0001-6468-6003; Email: yanjin19920602@xjtu.edu.cn

Yu Yao − *Department of Medical Oncology, The First Affiliated Hospital of Xi'an Jiaotong University, Xi'an 710061, China*; Email: yaoyu123@xjtufh.edu.cn

Wangxiao He − *Department of Medical Oncology, The First Affiliated Hospital of Xi'an Jiaotong University, Xi'an 710061, China; Department of Talent Highland, The First Affiliated Hospital of Xi'an Jiao Tong University, Xi'an 710061, China;* orcid.org/0000-0002-2054-6022; Email: hewangxiao5366@xjtu.edu.cn

Authors

Aimin Jiang − *Department of Medical Oncology, The First Affiliated Hospital of Xi'an Jiaotong University, Xi'an 710061, China*

Xiaoqiang Zheng − *Department of Medical Oncology, The First Affiliated Hospital of Xi'an Jiaotong University, Xi'an 710061, China; Institute for Stem Cell & Regenerative Medicine, The Second Affiliated Hospital of Xi'an Jiaotong University, Xi'an 710004, China*

Siqi Yan − *Institute for Stem Cell & Regenerative Medicine, The Second Affiliated Hospital of Xi'an Jiaotong University, Xi'an 710004, China*

Complete contact information is available at: https://pubs.acs.org/10.1021/acsnano.3c09852

Notes

The authors declare no competing financial interest.

ACKNOWLEDGMENTS

This work was supported by the National Natural Science Foundation of China (No. 82272782, No. 22007076, No. 32171256, No. 82141126), The National Key Research and Development Program of China (No. 2022YFE0133500), Thousand Talents Plan of Shaanxi Province (For W. He), the Key Research and development program of Shaanxi Province (No. 2020GXLH-Y-020), Innovation Capability Support Program of Shaanxi (Program No. 2021TD-44), and "The Young Talent Support Plan" of Xi'an Jiaotong University (For W. He). We would like to sincerely appreciate the Instrument Analysis Center of Xi'an Jiaotong University for their assistance with TEM, HRTEM, FT-IR, and DLS analysis. Besides, we also appreciate the help of RNA-*seq* analysis from Tgene Biotech (Shanghai) Co., Ltd.

REFERENCES

(1) Attili, I.; Tarantino, P.; Passaro, A.; Stati, V.; Curigliano, G.; de Marinis, F. Strategies to overcome resistance to immune checkpoint blockade in lung cancer. *Lung Cancer* **2021**, *154*, 151−160.

(2) Reck, M.; Rodriguez-Abreu, D.; Robinson, A. G.; Hui, R.; Csöszi, T.; Fülöp, A.; Gottfried, M.; Peled, N.; Tafreshi, A.; Cuffe, S.; O'Brien, M.; Rao, S.; Hotta, K.; Leiby, M. A.; Lubiniecki, G. M.; Shentu, Y.; Rangwala, R.; Brahmer, J. R. Pembrolizumab versus Chemotherapy for PD-L1-Positive Non-Small-Cell Lung Cancer. *N. Engl. J. Med.* **2016**, *375* (19), 1823−1833.

(3) Mok, T. S. K.; Wu, Y.-L.; Kudaba, I.; Kowalski, D. M.; Cho, B. C.; Turna, H. Z.; Castro, G.; Srimuninnimit, V.; Laktionov, K. K.; Bondarenko, I.; Kubota, K.; Lubiniecki, G. M.; Zhang, J.; Kush, D.; Lopes, G.; Adamchuk, G.; Ahn, M.-J.; Alexandru, A.; Altundag, O.; Alyasova, A.; et al. Pembrolizumab versus chemotherapy for previously untreated, PD-L1-expressing, locally advanced or metastatic non-small-cell lung cancer (KEYNOTE-042): a randomised, open-label, controlled, phase 3 trial. *Lancet* **2019**, *393* (10183), 1819−1830.

(4) Gandhi, L.; Rodríguez-Abreu, D.; Gadgeel, S.; Esteban, E.; Felip, E.; De Angelis, F.; Domine, M.; Clingan, P.; Hochmair, M. J.; Powell, S. F.; Cheng, S. Y. S.; Bischoff, H. G.; Peled, N.; Grossi, F.; Jennens, R. R.; Reck, M.; Hui, R.; Garon, E. B.; Boyer, M.; Rubio-Viqueira, B.; et al. Pembrolizumab plus chemotherapy in metastatic non-small-cell lung cancer. *N. Engl. J. Med.* **2018**, *378* (22), 2078−2092.

(5) Herbst, R. S.; Giaccone, G.; de Marinis, F.; Reinmuth, N.; Vergnenegre, A.; Barrios, C. H.; Morise, M.; Felip, E.; Andric, Z.; Geater, S.; Özgüroğlu, M.; Zou, W.; Sandler, A.; Enquist, I.; Komatsubara, K.; Deng, Y.; Kuriki, H.; Wen, X.; McCleland, M.; Mocci, S.; et al. Atezolizumab for first-line treatment of PD-L1-selected patients with NSCLC. *N. Engl. J. Med.* **2020**, *383* (14), 1328−1339.

(6) Suresh, K.; Naidoo, J.; Lin, C. T.; Danoff, S. Immune Checkpoint Immunotherapy for Non-Small Cell Lung Cancer: Benefits and Pulmonary Toxicities. *Chest* **2018**, *154* (6), 1416−1423.

(7) Segal, E. M. Immunotherapy in the frontline management of advanced and metastatic NSCLC. *Am. J. Manag. Care* **2021**, *27* (18 Suppl), S323−S332.

(8) Zhang, M.; Fan, Y.; Nie, L.; Wang, G.; Sun, K.; Cheng, Y. Clinical Outcomes of Immune Checkpoint Inhibitor Therapy in Patients With Advanced Non-small Cell Lung Cancer and Preexisting Interstitial Lung Diseases: A Systematic Review and Meta-analysis. *Chest* **2022**, *161* (6), 1675−1686.

(9) Doroshow, D. B.; Sanmamed, M. F.; Hastings, K.; Politi, K.; Rimm, D. L.; Chen, L.; Melero, I.; Schalper, K. A.; Herbst, R. S. Immunotherapy in Non-Small Cell Lung Cancer: Facts and Hopes. *Clin. Cancer. Res.* **2019**, *25* (15), 4592−4602.

(10) Xiong, W.; Zhao, Y.; Du, H.; Guo, X. Current Status of Immune Checkpoint Inhibitor Immunotherapy for Lung Cancer. *Front. Oncol.* **2021**, *11*, 704336.

(11) Atchley, W. T.; Alvarez, C.; Saxena-Beem, S.; Schwartz, T. A.; Ishizawar, R. C.; Patel, K. P.; Rivera, M. P. Immune Checkpoint Inhibitor-Related Pneumonitis in Lung Cancer: Real-World Incidence, Risk Factors, and Management Practices Across Six Health Care Centers in North Carolina. *Chest* **2021**, *160* (2), 731−742.

(12) Cho, J. Y.; Kim, J.; Lee, J. S.; Kim, Y. J.; Kim, S. H.; Lee, Y. J.; Cho, Y. J.; Yoon, H. I.; Lee, J. H.; Lee, C. T.; Park, J. S. Characteristics, incidence, and risk factors of immune checkpoint inhibitor-related pneumonitis in patients with non-small cell lung cancer. *Lung Cancer* **2018**, *125*, 150−156.

(13) Naidoo, J.; Wang, X.; Woo, K. M.; Iyriboz, T.; Halpenny, D.; Cunningham, J.; Chaft, J. E.; Segal, N. H.; Callahan, M. K.; Lesokhin, A. M.; Rosenberg, J.; Voss, M. H.; Rudin, C. M.; Rizvi, H.; Hou, X.; Rodriguez, K.; Albano, M.; Gordon, R. A.; Leduc, C.; Rekhtman, N.; et al. Pneumonitis in Patients Treated With Anti-Programmed Death-1/Programmed Death Ligand 1 Therapy. *J. Clin. Oncol.* **2017**, *35* (7), 709−717.

(14) Yin, J.; Wu, Y.; Yang, X.; Gan, L.; Xue, J. Checkpoint Inhibitor Pneumonitis Induced by Anti-PD-1/PD-L1 Therapy in Non-Small-Cell Lung Cancer: Occurrence and Mechanism. *Front. Immunol.* **2022**, *13*, 830631.

(15) Xiao, Y.; Yu, S.; Zhu, B.; Bedoret, D.; Bu, X.; Francisco, L. M.; Hua, P.; Duke-Cohan, J. S.; Umetsu, D. T.; Sharpe, A. H.; DeKruyff, R. H.; Freeman, G. J. RGMb is a novel binding partner for PD-L2 and its engagement with PD-L2 promotes respiratory tolerance. *J. Exp. Med.* **2014**, *211* (5), 943−59.

(16) Nie, X.; Chen, W.; Zhu, Y.; Huang, B.; Yu, W.; Wu, Z.; Guo, S.; Zhu, Y.; Luo, L.; Wang, S.; Chen, L. B7-DC (PD-L2) costimulation of CD4(+) T-helper 1 response via RGMb. *Cell. Mol. Immunol.* **2018**, *15* (10), 888−897.
(17) Tabchi, S.; Messier, C.; Blais, N. Immune-mediated respiratory adverse events of checkpoint inhibitors. *Curr. Opin. Oncol.* **2016**, *28* (4), 269.
(18) Ohaegbulam, K. C.; Assal, A.; Lazar-Molnar, E.; Yao, Y.; Zang, X. Human cancer immunotherapy with antibodies to the PD-1 and PD-L1 pathway. *Trends Mol. Med.* **2015**, *21* (1), 24−33.
(19) Sharpe, A. H.; Pauken, K. E. The diverse functions of the PD1 inhibitory pathway. *Nat. Rev. Immunol.* **2018**, *18* (3), 153−167.
(20) Cong, V. T.; Houng, J. L.; Kavallaris, M.; Chen, X.; Tilley, R. D.; Gooding, J. J. How can we use the endocytosis pathways to design nanoparticle drug-delivery vehicles to target cancer cells over healthy cells? *Chem. Soc. Rev.* **2022**, *51* (17), 7531−7559.
(21) Ng, C. T.; Tang, F. M.; Li, J. J.; Ong, C.; Yung, L. L.; Bay, B. H. Clathrin-mediated endocytosis of gold nanoparticles in vitro. *Anat. Rec.* **2015**, *298* (2), 418−27.
(22) He, W.; Zhang, Z.; Yang, W.; Zheng, X.; You, W.; Yao, Y.; Yan, J.; Liu, W. Turing milk into pro-apoptotic oral nanotherapeutic: De novo bionic chiral-peptide supramolecule for cancer targeted and immunological therapy. *Theranostics* **2022**, *12* (5), 2322−2334.
(23) He, W.; Yan, J.; Li, Y.; Yan, S.; Wang, S.; Hou, P.; Lu, W. Resurrecting a p53 peptide activator - An enabling nanoengineering strategy for peptide therapeutics. *J. Controlled Release* **2020**, *325*, 293−303.
(24) Yan, S.; Yan, J.; Liu, D.; Li, X.; Kang, Q.; You, W.; Zhang, J.; Wang, L.; Tian, Z.; Lu, W.; Liu, W.; He, W. A nano-predator of pathological MDMX construct by clearable supramolecular gold(I)-thiol-peptide complexes achieves safe and potent anti-tumor activity. *Theranostics* **2021**, *11* (14), 6833−6846.
(25) Yan, J.; Ji, F.; Yan, S.; You, W.; Ma, F.; Li, F.; Huang, Y.; Liu, W.; He, W. A general-purpose nanohybrid fabricated by polymeric Au(I)-peptide precursor to wake the function of peptide therapeutics. *Theranostics* **2020**, *10* (19), 8513−8527.
(26) Yang, W.; Liu, W.; Li, X.; Yan, J.; He, W. Turning chiral peptides into a racemic supraparticle to induce the self-degradation of MDM2. *J. Adv. Res.* **2023**, *45*, 59−71.
(27) Song, M.; Dong, S.; An, X.; Zhang, W.; Shen, N.; Li, Y.; Guo, C.; Liu, C.; Li, X.; Chen, S. Erythrocyte-biomimetic nanosystems to improve antitumor effects of paclitaxel on epithelial cancers. *J. Controlled Release* **2022**, *345*, 744−754.
(28) Yamaguchi, T.; Shimizu, J.; Hasegawa, T.; Horio, Y.; Inaba, Y.; Yatabe, Y.; Hida, T. Pre-existing pulmonary fibrosis is a risk factor for anti-PD-1-related pneumonitis in patients with non-small cell lung cancer: A retrospective analysis. *Lung Cancer* **2018**, *125*, 212−217.
(29) Cadranel, J.; Canellas, A.; Matton, L.; Darrason, M.; Parrot, A.; Naccache, J.-M.; Lavolé, A.; Ruppert, A.-M.; Fallet, V. Pulmonary complications of immune checkpoint inhibitors in patients with nonsmall cell lung cancer. *European Respiratory Review* **2019**, *28* (153), 190058.
(30) Rashdan, S.; Minna, J. D.; Gerber, D. E. Diagnosis and management of pulmonary toxicity associated with cancer immunotherapy. *Lancet Respiratory Medicine* **2018**, *6* (6), 472−478.
(31) Li, S.; Shi, J.; Tang, H. Animal models of drug-induced pulmonary fibrosis: an overview of molecular mechanisms and characteristics. *Cell Biology And Toxicology* **2022**, *38* (5), 699−723.
(32) Petitprez, F.; Levy, S.; Sun, C. M.; Meylan, M.; Linhard, C.; Becht, E.; Elarouci, N.; Tavel, D.; Roumenina, L. T.; Ayadi, M.; Sautès-Fridman, C.; Fridman, W. H.; de Reyniès, A. The murine Microenvironment Cell Population counter method to estimate abundance of tissue-infiltrating immune and stromal cell populations in murine samples using gene expression. *Genome Med.* **2020**, *12* (1), 86.
(33) Li, L.; He, W.; You, W.; Yan, J.; Liu, W. Turing miRNA into infinite coordination supermolecule: a general and enabling nano-engineering strategy for resurrecting nuclear acid therapeutics. *J. Nanobiotechnol.* **2022**, *20* (1), 1−15.
(34) Bian, Z.; Yan, J.; Wang, S.; Li, Y.; Guo, Y.; Ma, B.; Guo, H.; Lei, Z.; Yin, C.; Zhou, Y.; Liu, M.; Tao, K.; Hou, P.; He, W. Awakening p53 in vivo by D-peptides-functionalized ultra-small nanoparticles: Overcoming biological barriers to D-peptide drug delivery. *Theranostics* **2018**, *8* (19), 5320−5335.
(35) Zheng, X.; Yan, J.; You, W.; Li, F.; Diao, J.; He, W.; Yao, Y. De novo nano-erythrocyte structurally braced by biomimetic Au(I)-peptide skeleton for MDM2/MDMX predation toward augmented pulmonary adenocarcinoma immunotherapy. *Small* **2021**, *17* (20), e2100394.
(36) Heinrich, R.; Gaestel, M.; Glaser, R. The electric potential profile across the erythrocyte membrane. *J. Theor. Biol.* **1982**, *96* (2), 211−231.
(37) Oldenborg, P. A.; Zheleznyak, A.; Fang, Y. F.; Lagenaur, C. F.; Gresham, H. D.; Lindberg, F. P. Role of CD47 as a marker of self on red blood cells. *Science* **2000**, *288* (5473), 2051−4.
(38) Su, Z.; Dong, S.; Chen, Y.; Huang, T.; Qin, B.; Yang, Q.; Jiang, X.; Zou, C. Microfluidics-Enabled Nanovesicle Delivers CD47/PD-L1 Antibodies to Enhance Antitumor Immunity and Reduce Immunotoxicity in Lung Adenocarcinoma. *Adv. Sci.* **2023**, *10* (20), e2206213.
(39) Ikeda, S.; Kato, T.; Kenmotsu, H.; Ogura, T.; Iwasawa, S.; Sato, Y.; Harada, T.; Kubota, K.; Tokito, T.; Okamoto, I.; Furuya, N.; Yokoyama, T.; Hosokawa, S.; Iwasawa, T.; Yamanaka, T.; Okamoto, H. A Phase 2 Study of Atezolizumab for Pretreated NSCLC With Idiopathic Interstitial Pneumonitis. *J. Thorac. Oncol.* **2020**, *15* (12), 1935−1942.
(40) Ikeda, S.; Kato, T.; Kenmotsu, H.; Ogura, T.; Iwasawa, S.; Iwasawa, T.; Kasajima, R.; Miyagi, Y.; Misumi, T.; Yamanaka, T.; Okamoto, H. A phase II study of atezolizumab for pretreated advanced/recurrent non-small cell lung cancer with idiopathic interstitial pneumonias: rationale and design for the TORG1936/AMBITIOUS study. *Ther. Adv. Med. Oncol.* **2020**, *12*, 175883592092202.
(41) Krishnan, N.; Jiang, Y.; Zhou, J.; Mohapatra, A.; Peng, F. X.; Duan, Y.; Holay, M.; Chekuri, S.; Guo, Z.; Gao, W.; Fang, R. H.; Zhang, L. A modular approach to enhancing cell membrane-coated nanoparticle functionality using genetic engineering. *Nat. Nanotechnol.* **2023**, DOI: 10.1038/s41565-023-01533-w.
(42) Anstee, D. J. The relationship between blood groups and disease. *Blood* **2010**, *115* (23), 4635−4643.
(43) de Oliveira, S.; Saldanha, C. An overview about erythrocyte membrane. *Clin Hemorheol Microcirc* **2010**, *44* (1), 63−74.
(44) Jiang, A.; Liu, N.; Wang, J.; Zheng, X.; Ren, M.; Zhang, W.; Yao, Y. The role of PD-1/PD-L1 axis in idiopathic pulmonary fibrosis: Friend or foe? *Front. Immunol.* **2022**, DOI: 10.3389/fimmu.2022.1022228.
(45) Li, S.; Shi, J.; Tang, H. Animal models of drug-induced pulmonary fibrosis: an overview of molecular mechanisms and characteristics. *Cell Biol. Toxicol* **2022**, *38* (5), 699−723.
(46) Pan, T.; Zhou, Q.; Miao, K.; Zhang, L.; Wu, G.; Yu, J.; Xu, Y.; Xiong, W.; Li, Y.; Wang, Y. Suppressing Sart1 to modulate macrophage polarization by siRNA-loaded liposomes: a promising therapeutic strategy for pulmonary fibrosis. *Theranostics* **2021**, *11* (3), 1192−1206.

https://doi.org/10.1021/acsnano.3c09852
ACS Nano 2024, 18, 5358−5373